Imaging of supersonic flow over a double elliptic surface*

Zhang Qing-Hu(张庆虎), Yi Shi-He(易仕和), He Lin(何 霖)†,
Zhu Yang-Zhu(朱杨柱), and Chen Zhi(陈 植)

College of Aerospace Science and Engineering, National University of Defense Technology, Changsha 410073, *China*

(Received 22 January 2013; revised manuscript received 13 May 2013)

The coherent structures of flow over a double elliptic surface are experimentally investigated in a supersonic low-noise wind tunnel at Mach number 3 using nano-tracer planar laser scattering (NPLS) and particle image velocimetry (PIV) techniques. High spatiotemporal resolution images and velocity fields of both laminar and turbulent inflows over the test model are captured. Based on the time-correlation images, the spatial and temporal evolutionary characteristics of the coherent structures are investigated. The flow structures in the NPLS images are in good agreement with the velocity fluctuation fields by PIV. From statistically significant ensembles, spatial correlation analysis of both cases is performed to quantify the mean size and the orientation of coherent structures. The results indicate that the mean structure is elliptical in shape and the structural angles in the separated region of laminar inflow are slightly smaller than that of turbulent inflow. Moreover, the structural angles of both cases increase with their distance away from the wall.

Keywords: coherent structures, separated flow, spatial correlation analysis, supersonic flow

PACS: 47.27.De, 47.32.Ff, 47.40.Ki, 47.80.Cb **DOI:** 10.1088/1674-1056/22/11/114703

1. Introduction

Separated flows have been the subject of experimental and computational research for decades because of their practical importance in many common supersonic aircrafts. Supersonic separated flows generated by a two-dimensional (2D) compression curved surface contain several characteristics that are quite formidable for accurate Computational Fluid Dynamics (CFD) modeling and prediction. These characteristics involve the presence of shock waves, a recirculation region adjacent to the model, and thin compressible shears layer with steep gradients of the physical variables. Therefore, experimental research in this area is crucial for gaining a better understanding of the physical phenomena that dominate these high-speed separated flows.[1] Schlieren and shadowgraph approaches have been extensively used in the investigation of compressible separated and shear flows. However, these techniques cannot accurately determine the transient structures because the fine structures are blurred by the spatial integration along the line-of-sight. In order to obtain the instantaneous structures, a different technique should be utilized.

In the last two decades, filtered Rayleigh scattering (FRS) and condensate-enhanced Rayleigh scattering have been used extensively in the study of the compressible separated and shear flows.[1–8] Dutton *et al.*[1,2] experimentally investigated the spatial evolution of large-scale structures in the shear layer of a supersonic base flow and an axisymmetric supersonic separated flow. The results of their studies showed that the mean side-view structure was highly strained and inclined toward the local free stream direction. Bookey *et al.*[5,8] experimentally investigated the flow in Mach 2.9 shock wave turbulent boundary layer interaction generated by a 2D compression ramp. They provided quantitative measurements of the turbulent structural angle and other parameters. Very recently, Humble *et al.*[6] visualized and analyzed a Mach 4.9 turbulent boundary layer. Particle image velocimetry (PIV) is another tool for the study of supersonic separated and shear flows.[7–10]

Coherent structures play a major role in the dynamics of turbulent flows in the cases of both free-shear and wall-bounded flows.[11] These structures are responsible for the transport of low-momentum fluid and for the Reynolds-stress production. The vortex organization in wall turbulence has been extensively studied,[12–21] however, most studies focus on the zero pressure gradient boundary layer. Because of the compressibility effectsl[22,23] the adverse pressure gradient boundary layer of supersonic flow over a curved surface would generate more complex flows.

Nano-tracer planar laser scattering (NPLS) is a new flow visualization technique for measuring the fine structures of a supersonic flow.[24] In the present work, the supersonic flow over a double elliptic surface is experimentally investigated using NPLS and PIV techniques. The rest of the paper is organized as follows. In Section 2, the flow facility and NPLS technique are described in detail. The flow imaging and velocity fields of laminar and fully developed turbulent inflows over the test model are given in Section 3. Spatial correlation analysis of large ensembles of images is performed in Section 4. Conclusions drawn from the present work are summarized in Section 5.

*Project supported by the National Natural Science Foundation of China (Grant No. 11172326), the National Basic Research Program of China (Grant No. 2009CB724100), and the Scientific Research Program of National University of Defense Technology, China (Grant No. 0100010112001).

†Corresponding author. E-mail: helin.101sys@gmail.com

© 2013 Chinese Physical Society and IOP Publishing Ltd

2. Experimental apparatus

2.1. Flow facility

A set of experiments were performed in a supersonic low-noise wind tunnel at Mach number 3 (Fig. 1). The total temperature T_0 is 300 K and the total pressure P_0 is 101 kPa. The experimental parameters are given in Table 1, where Ma_∞, Re, and U_∞ are the Mach number, Reynold number, and velocity, respectively. The total temperature is 300 K and the total pressure is 101 kPa. The experimental parameters are given in Table 1. The dimensions of the test section are 120-mm in height, 100-mm in width, and 250-mm in length. The double elliptic surface is an intersection of two ellipses, half the major axes and half the minor axes of which are (79 mm, 20 mm) and (46 mm, 33 mm), respectively. The test model is 108-mm long, 33-mm high, and 100-mm wide. Note that the width of the model is the same as that of the test section; therefore, the flow field at mid-span can be considered to be 2D. The test model is placed on a flat plate. The schematic illustration of experimental arrangements is presented in Fig. 2. The distance between the leading edging of the flat plate the leading edge of the test model is 100 mm for the laminar inflow and 400 mm for the turbulent inflow.

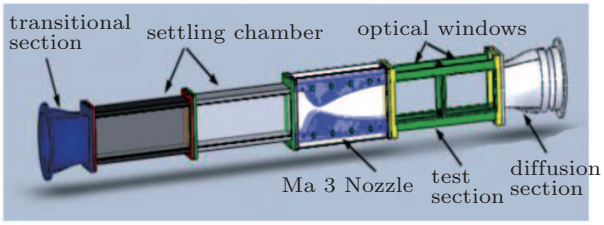


Fig. 1. (color online) Schematic diagram of the Mach 3 low-noise wind tunnel.

Table 1. Experimental parameters.

Ma_∞	T_0/K	P_0/kPa	Re/m^{-1}	U_∞/m·s^{-1}
3.0	300	101	7.5×10^6	620

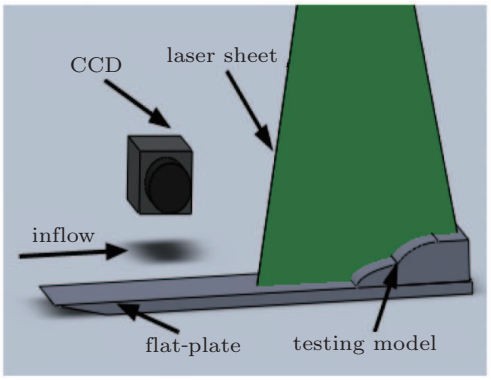


Fig. 2. (color online) Schematic illustration of experimental arrangements.

2.2. NPLS technique

NPLS is a new technique for flow imaging that uses nanoparticles as the tracer particles.[25] It has been used to investigate the supersonic mixing layer, boundary layer, aero-optics, and so forth.[24–31] As shown in Fig. 3, the NPLS system is composed of a nanoparticle generator, a dual-cavity Nd:YAG laser, an interline transfer double-exposure CCD camera, a synchronizer, and a computer. The laser with 500-mJ pulsed energy at the wavelength of 532 nm and 8-ns pulse duration is used as a light source. The laser beam is transformed into a uniform light sheet with the thickness less than 0.5 mm by a set of cylindrical lenses. The flow is imaged by using an interline transfer CCD camera with the resolution of 2048×2048 pixels. Two frames of a supersonic flow are recorded within a double-expose interval, which can be short as 200 ns.

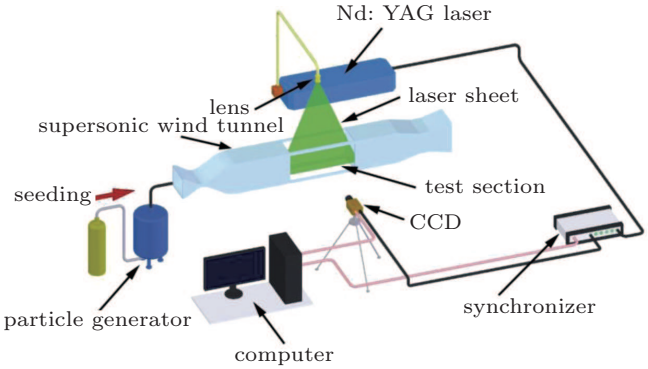


Fig. 3. (color online) Schematic diagram of the NPLS system.

3. Flow visualization and velocity fields

In this section, the results are categorized by the state of the incoming boundary layer, which is laminar and turbulent, respectively.

3.1. Laminar inflow

An instantaneous image of Mach 3 laminar inflow over the model is shown in Fig. 4. The origin $x = 0$ is located at the leading edge of the flat plate. The distance between the leading edge of the flat plate and the leading edge of the model is 100 mm. The incoming laminar boundary layer, a series of compression waves (marked as C), shock waves (labeled as S_1, S_2, and S), the separated flow upstream of the model, and the turbulent boundary layer at the test model can be identified clearly. Compression waves C are generated by the separated flow. Shock waves S_1 and S_2 are caused by the first elliptic surface as well as the boundary layer reattachment and the second elliptic surface, respectively. In the downstream region, compression waves C and shock waves S_1 merge into a stronger shock S. Moreover, the angle of the shock S locates between the angle of shock S_1 and the average angle of compression

waves C. At the beginning of the inflow (upstream of approximately 70 mm in Fig. 4), the flow at the flat plate is a thin laminar boundary layer with almost linear growth. In downstream region, the boundary layer transition begins to occur at approximately 73 mm in Fig. 4, however, previous results showed that the length of a laminar flow on the flat plate was about 180 mm under the same experimental conditions.[25] In a further downstream region, the boundary layer on the test model contains more small-scale structures, which indicates that the flow is turbulent. The size of coherent structures in the first curved surface is small, while it has a sharp increase in the second surface. The large-scale structures in the second surface are obviously intermittent.

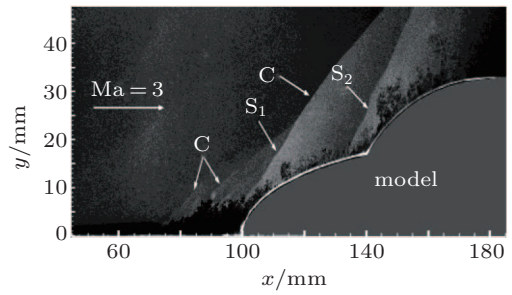


Fig. 4. Instantaneous image of Mach 3 laminar inflow over the model.

An higher resolution pair of images displaying the separation region with a delay of 1 μs is presented in Fig. 5. The structures in the outer layer and the center region can be identified clearly, whereas the bottom layer is blurred by the scattering irradiance from the flat plate. Because of the separated flow, the boundary layer transition occurs sharply. Structure A is elliptical in shape and inclined to the local streamwise axis. Structure B is a filament and also inclined to the local streamwise direction. It is noted that inclination angles of both structures A and B are less than 45°. The structure characteristics are similar to those of boundary layer transition for a zero pressure gradient flat plate. After 1 μs, structure A cannot be identified and structure B becomes very thin. It indicates that the boundary layer is unstable and coherent structures alter rapidly at the beginning of the transition. Structure C detaches from the main boundary layer, and exhibits an irregular polygonal shape. Structure D is a very large-scale structure. Moreover, there are many small-scale structures around its periphery. The inclination angles of vortices C and D are rather close to 90° to the wall, greatly larger than that at the beginning of the transition. With a delay of 1 μs, structure C maintains most of its shape characteristics and enlarges slightly, whereas structure D remains almost intact. Large-scale structures prevail in the center of the separation region. Structures E and F are elliptical structures with an inclination angle approximately 45° to the free-stream streamwise axis. Moreover these structures are very similar to those of flat plate boundary layer.[13,26] After 1 μs, structures E and F retain most their shape characteristics and are slightly distorted. Structure E has a streamwise displacement, while vortex F has a reverse motion of approximately −0.15 mm.

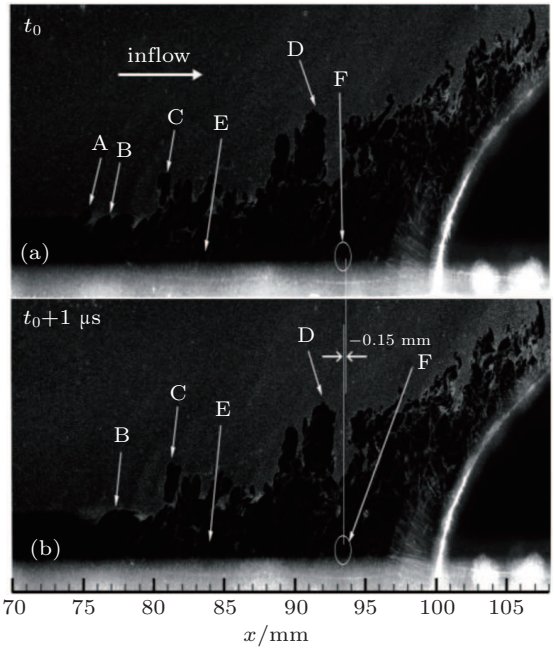


Fig. 5. Higher resolution pair of images displaying the separation region with a delay of 1 μs. (a) The first image, (b) the second image.

3.2. Turbulent inflow

Figure 6 presents an instantaneous image of Mach 3 fully developed turbulent inflow over the test model. The origin $x = 0$ is located at the leading edge of the model. The distance between the leading edge of the flat plate and the leading edge of the model is 400 mm, which ensures that the incoming flow is a fully developed turbulent boundary layer.[26] Shock waves marked as S_1, S_2, S_3, and S_4 are generated by separated flow, the first curved surface, reattachment of the boundary layer, and the second elliptic surface, respectively. Compared with the shock S_1, shocks S_2 and S_3 are fairly weak, and moreover the three shocks merged into a strong shock (marked as S). It can be seen that the incoming boundary layer is characteristic of small-scale structures, so it indicates that it has been fully developed turbulence.[25] Previous studies suggest that the motion of the instantaneous separation point is closely tied to the instantaneous position of the shock.[32] By extrapolating the shock with a straight line to the flat plate location, the position of the shock foot is approximately 21.5 mm upstream of the leading edge of the model in the flow direction. According to this estimating method, the extent of the instantaneous separated region is from $x = -21.5$ mm to the origin in Fig. 6. At the beginning of the first elliptic surface, the boundary layer is irregular. However, regular large-scale structures (marked as A and B) are seen from about the middle of the first elliptic surface, and moreover they survive over the second elliptic surface (such as structures C and D). These structures are

characteristic of an inclined structure upstream of the spanwise vortex connecting the vortex core with the wall. Based on the known characteristics of the hairpin vortex in the streamwise-wall-normal plane,[13,25] the present structures can be readily treated as hairpin vortices.

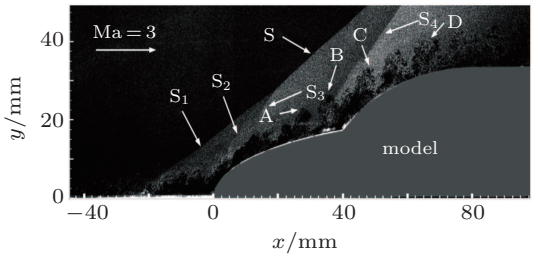


Fig. 6. An instantaneous image of Mach 3 fully developed turbulent inflow over the model.

3.3. Velocity fields

Figure 7 shows the average velocity distribution of Mach 3 flow, including laminar and turbulent inflows, over the test model. Both of the origins are located at the leading edge of the model. The recirculation zone exists upstream of the test model in both cases. The extent of the recirculation zone of the laminar inflow is much larger than that of the turbulent inflow. It is consistent with the results of flow imaging. Moreover, compared with Figs. 4 and 6, shock waves can be clearly identified because of the sharp velocity variance across the shock waves.

Instantaneous velocity fluctuation fields of Mach 3 flow, including laminar and turbulent inflows, over the test model are shown in Fig. 8. It can be seen that the strongest velocity fluctuation occurs around the location of separation point (approximately $x = -50$ mm in Fig. 8(a) and $x = -20$ mm in Fig. 8(b) and reattachment region (marked as A in Fig. 8(a) and D in Fig. 8(b)). Also, there is strong velocity fluctuation in the boundary layer because of the motions of large-scale structures. Comparing Fig. 8(a) with Fig. 4, there is velocity fluctuation around shock waves (S_1 and S_2 in Fig. 8(a)). There is weak velocity fluctuation downstream the first surface of the model, corresponding to the thin boundary layer at this location in Fig. 4. Moreover, the scope of velocity fluctuation sharply increases in the middle of the second surface, corresponding to the occurrence of the very large structures at this location in Fig. 4. Comparing Fig. 8(b) with Fig. 6, the scope of velocity fluctuation abruptly increases at the middle of the first surface, corresponding to the occurrence of the regular large-scale structures at this location. In addition, there is velocity fluctuation around the shock wave (marked as C_1 in Fig. 8(b)).

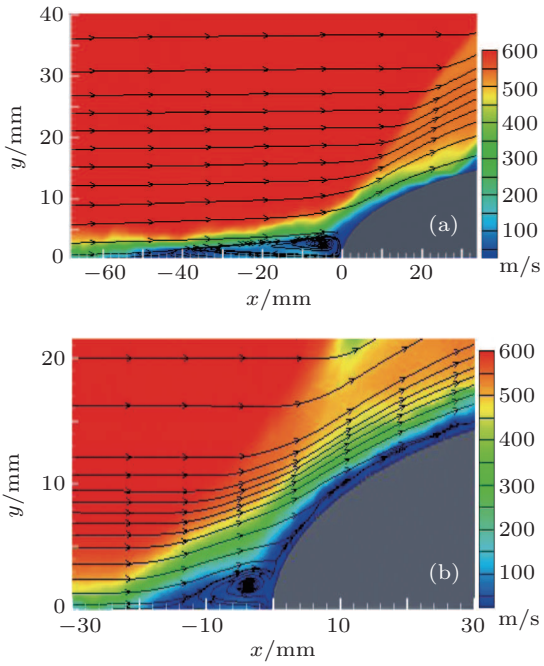


Fig. 7. (color online) Average velocity distribution of Mach 3 flow over the test model: (a) laminar inflow, (b) turbulent inflow.

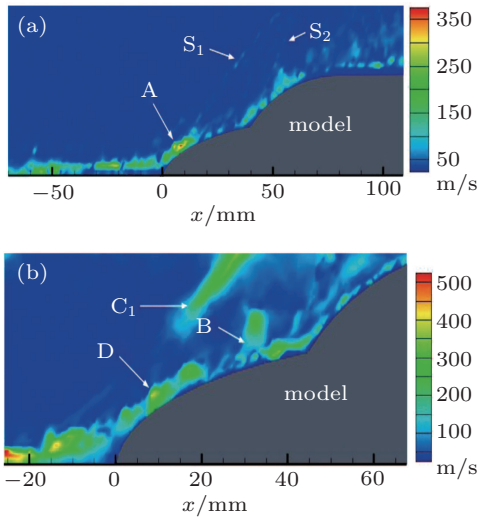


Fig. 8. (color online) Instantaneous velocity fluctuation fields of Mach 3 flow over the test model: (a) laminar inflow; (b) turbulent inflow.

4. Spatial correlation analysis

To quantify the average spatial features of coherent structures, two-point spatial correlation functions are evaluated statistically according to

$$R(i,j) = \frac{\sum_{n=1}^{N} (I_n(i,j) - \bar{I}(i,j))(I_n(i_0,j_0) - \bar{I}(i_0,j_0)}{\sqrt{\sum_{n=1}^{N} (I_n(i,j) - \bar{I}(i,j))^2 \sum_{n=1}^{N} (I_n(i_0,j_0) - \bar{I}(i_0,j_0))^2}}, \quad (1)$$

where I_n is the gray value of the n-th sample image, i an j are pixels coordinates, 0 denotes a reference coordinate, and the over bar represents the mean value. Previous studies indicated that an ensemble of 512 images ensured stable statistic results,[1] therefore, image ensembles of over this size are used in the present work.

4.1. Laminar inflow

Four different points are selected as the reference position, namely, $(x_0, y_0) = (75, 2.8)$, (85, 3.6), (95, 4.1), (95, 3.1), respectively, corresponding to the coordinates in Fig. 4. The first three reference points are selected as $y_0/\delta_{\text{local}} = 0.75$ (δ_{local} is the local boundary layer thickness), and the last point is located inside the recirculation zone. Figure 9 shows the contour plots of spatial correlation fields at the above four reference points, computed from an ensemble of 520 images. For each of the correlation fields, iso-correlation values are from 0.5 in even increments of 0.1 to the central peak, which has a value of unity by definition. Consistent with other flow imaging studies,[1,7] correlation contours exhibit an elliptical property. Note that the iso-correlations represent the average structures of coherent motions. The 0.5 contour level is used to determine the mean structural size and mean structural angle θ, as the same contour used by Bourdon *et al.*,[1] thus ellipses are fitted to this iso-correlation contour using a direct least-square-fitting method originated from Fitzgibbon *et al.*[33]

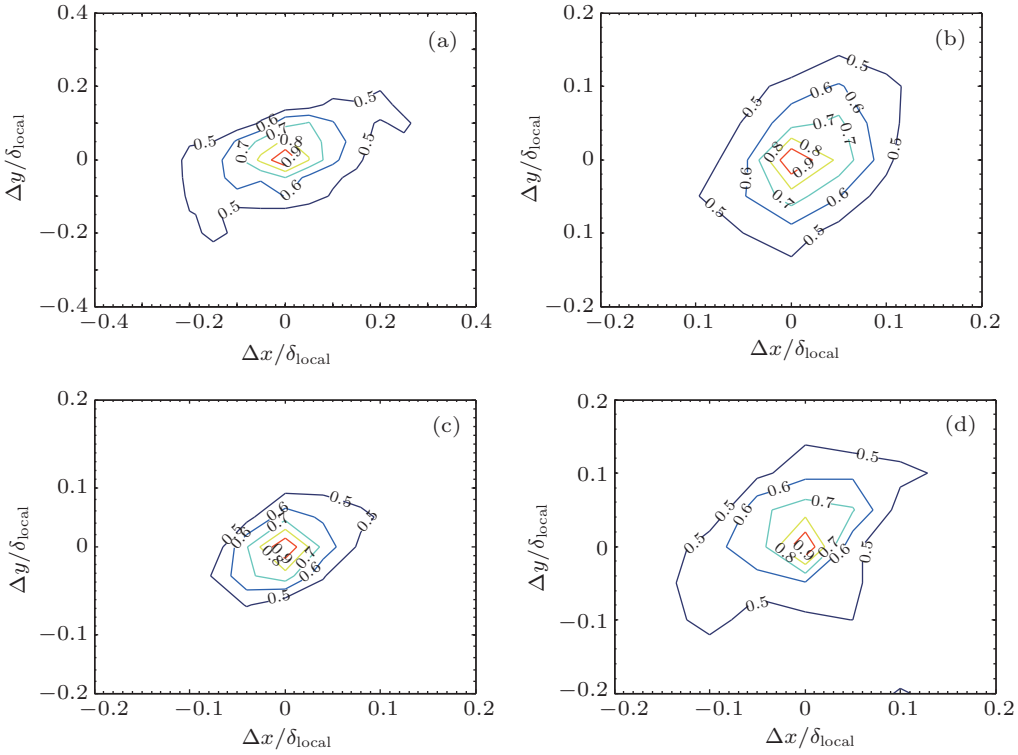


Fig. 9. (color online) Spatial correlation fields of four reference points, contours are at 0.1 intervals from 0.5 to 0.9, the coordinates of these points are: (a) (75, 2.8), (b) (85, 3.6), (c) (95, 4.1), (d) (95, 3.1).

Table 2 presents the reference points' parameters and the fundamental statistics describing correlation fields of Fig. 9. The (x_0, y_0) is the coordinate value of the reference point; δ_{local} is the local boundary layer thickness; a is the major axis of the fitting ellipse; θ is the structural angle (defined as the angle between the flat plate and the major axis of the fitting ellipse). Immediately following the flow separation (position I), structural angle θ is relatively small and the average size of the structures is quite large. In the downstream region (points II, III, and IV), the structural angles are all approximately 45°. Moreover, the average size of the structures is relatively small, which indicates that the structures are large at the beginning of the separated region and exhibit small-scale characteristics in the downstream region. The average size of the structures in the interior of the recirculation zone (point IV) is larger than that in the outer layer (point III) at the same streamwise place.

Table 2. Parameters of reference points and spatial correlation results of Fig. 9.

Position	x_0/mm	y_0/mm	δ_{local}/mm	a/mm	a/δ_{local}	θ/(°)
I	78	2.8	3.7	1.77	0.48	23.6
II	85	3.6	4.8	1.08	0.22	48.7
III	95	4.1	5.5	0.88	0.16	38.5
IV	95	3.3	5.5	1.43	0.26	36.8

4.2. Turbulent inflow

Two different points are selected as the reference position, i.e., $(x_0, y_0) = (-25, 5.6), (-5, 7.0)$, respectively, corresponding to the coordinates in Fig. 6. The reference points are

selected as $y_0/\delta_{\text{local}} = 0.75$ (δ_{local} is the local boundary layer thickness). Contour plots of spatial correlation fields at the two reference points, computed from an ensemble of 550 images, are shown in Fig. 10. For each of the correlation fields, iso-correlation values are from 0.5 in even increments of 0.1 to the central peak. In addition, the 0.5 contour level is used for the determination of the mean structural size and the mean structural angle θ. The two reference points' parameters and the fundamental statistics describing the correlation fields of Fig. 10 are given in Table 3.

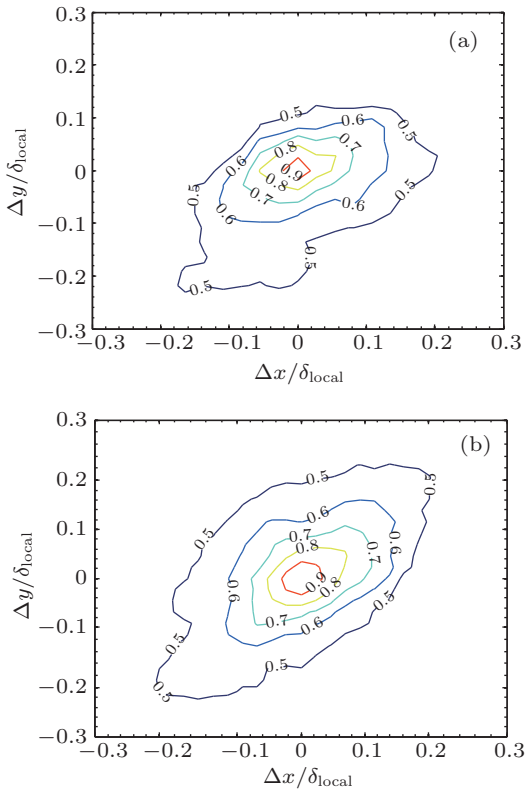


Fig. 10. (color online) Spatial correlation fields of two reference points, contours are at 0.1 intervals from 0.5 to 0.9, the coordinates of these points are: (a) $(-25, 5.6)$, (b) $(-5, 7.0)$.

Table 3. Parameters of reference points and spatial correlation results of Fig. 10.

Position	x_0/mm	y_0/mm	δ_{local}/mm	a/mm	a/δ_{local}	θ/(°)
I	–25	5.6	7.4	2.69	0.36	35.3
II	–5	7.0	9.3	3.70	0.40	43.2

Figure 11 shows the structural angle versus non-dimensional height of the boundary layer, located 5 mm upstream of the leading edge of the test model. Results calculated from FRS images in a similar position of compression corner at Mach 2.9 in Ref. [8] are shown for comparison. An accurate evaluation for $y/\delta < 0.5$ is not possible because of the loss of signal in the lower half of the boundary layer. The results show a range of structural angles of turbulent inflow from 40° to 55°, in good agreement with that at Mach 2.9 in Ref. [8]. The structural angles in the separated region of laminar inflow are slightly smaller than that of the turbulent inflow. Moreover, the structural angle of both laminar and turbulent inflows increases with its distance to the wall, which is consistent with previous studies.[6,8]

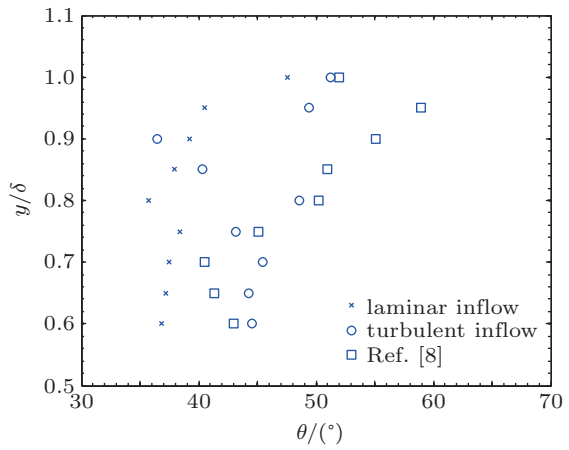


Fig. 11. (color online) Structural angle versus non-dimensional height of the boundary layer, located upstream 5 mm of the leading edge of the test model, results by FRS images in similar position of compression corner at Mach 2.9 in Ref. [8] shown for comparison.

5. Conclusion

Coherent structures of supersonic flow over a double elliptic surface are experimentally investigated in a supersonic low-noise wind tunnel at Mach number 3 using NPLS and PIV techniques. The incoming boundary layer includes laminar and turbulent inflows. High spatiotemporal resolution images and velocity fields of supersonic flow over the test model are captured. The fine structures of both cases are revealed and investigated. The results of laminar inflow show that the boundary layer transition occurs rapidly upstream of the test model because of the separated flow. The size of coherent structures in the first surface of the test model is small, whereas it has an sharp increase in the second surface. The results of fully developed turbulent inflow show that the boundary layer displays large-scale structures downstream of the middle of the first elliptic surface. Moreover, the coherent structures in the second elliptic surface of both laminar and turbulent inflows are obvious intermittent. The results of flow imaging show that the extent of separated region of laminar inflow is larger than that of the turbulent inflow. Furthermore, it is confirmed by the results of PIV. The flow structures in the NPLS images are in good agreement with the velocity fluctuation fields by PIV.

Spatial correlation analysis is performed over a large ensemble of images in the separated region of both laminar and turbulent inflows. The mean structures are shown to be elliptical and inclined toward the local flow direction. The structural angles in the separated region of turbulent inflow are slightly larger than those of laminar inflow. The structural angle of both laminar and turbulent inflows increases with its distance away from the wall.

References

[1] Bourdon C J and Dutton J C 1999 *Phys. Fluids* **11** 201
[2] Smith K M and Dutton J C 1996 *AIAA J.* **34** 1146
[3] Papamoschou D and Bunyajitradulya A 1997 *Phys. Fluids* **9** 756
[4] Poggie J, Erbland P J, Smits A J and Miles R B 2004 *Exp. Fluids* **37** 438
[5] Bookey P, Wyckham C, Smits A J and Martin M P 2005 43*rd Aerospcae Sciences Meeting and Exhibit*, 10–13 January, 2005, Reno, USA, AIAA 2005-309
[6] Humble R A, Peltier S J, Lynch, Thurow B S and Bowersox 2011 41*st AIAA Fluid Dynamics Conference and Exhibit*, 27–30 June, 2011, Hawaii, USA, AIAA 2011-3419
[7] Ganapathisubramani B, Clemens N T and Dolling D S 2007 *J. Fluid Mech.* **585** 369
[8] Ringuette M J, Bookey P, Wyckham C and Smits A J 2009 *AIAA J.* **47** 373
[9] Hou Y X 2003 *Particle Image Velocimetry Study of Shock-induced Turbulent Boundary Layer Separation* (Ph. D. Dissertation) (Austin: University of Texas)
[10] Schrijer F F J, Scarano F and van Oudheusden B W 2006 *Exp. Fluids* **41** 353
[11] Pirozzoli S, Bernardini M and Grasso F 2010 *J Fluid. Mech.* **648** 325
[12] Adrian R J, meinhart C D and Tomkins C D 2000 *J Fluid. Mech.* **422** 1
[13] Adrian R J 2007 *Phys. Fluids* **19** 041301
[14] Pirozzoli S, Bernardini M and Grasso F 2008 *J Fluid Mech.* **613** 205
[15] Schülein E and Trofimov V M 2011 *J Fluid. Mech.* **672** 451
[16] Zhang C, Pan C and Wang J J 2011 *Exp. Fluids* **51** 1343
[17] Tang Z Q, Jiang N, Schröder A and Geisler R 2012 *Acta Mech. Sin.* **28** 572
[18] Lee C B and Fu S 2000 *Chin. Phys.* **9** 508
[19] Li F C, Cai W H, Zhang H N and Wang Y 2012 *Chin. Phys. B* **21** 114701
[20] She Z S, Hu N and Wu Y 2009 *Acta Mech. Sin.* **25** 731
[21] Zhou Y, Ma Y W and Liang X L 2007 *Chin. Phys. Lett.* **24** 147
[22] Cao Y H, Pei J, Chen J and She Z S 2008 *Chin. Phys. Lett.* **25** 3315
[23] Wang L and Lu X Y 2011 *Chin. Phys. Lett.* **28** 034703
[24] Zhu Y Z, Yi S H, He L, Tian L F and Zhou Y W 2013 *Chin. Phys. B* **22** 014702
[25] Zhao Y X, Yi S H, Tian L F and Cheng Z Y 2009 *Sci. China Ser. E* **52** 3640
[26] He L, Yi S H, Zhao Y X, Tian L F and Chen Z 2011 *Chin. Sci. Bull.* **56** 489
[27] Gao Q, Yi S H, Jiang Z F and Xie W K 2012 *Chin. Phys. B* **21** 064701
[28] Wang B, Liu W D, Zhao Y X, Fan X Q and Wang C 2012 *Phys. Fluids* **24** 055110
[29] Chen Z, Yi S H, Tian L F, He L and Zhu Y Z 2012 *Shock Waves* **23** 299
[30] He L, Yi S H, Tian L F, Chen Z and Zhu Y Z 2013 *Chin. Phys. B* **22** 024704
[31] Zhu Y Z, Yi S H, Chen Z, Ge Y, Wang X H and Fu J 2013 *Acta Phys. Sin.* **6** 084219 (in Chinese)
[32] Smits A J and Dussauge J P 2006 *Turbulent Shear Layers in Supersonic Flow* 2nd edn. (New York: Springer) pp. 323–325
[33] Fitzgibbon A W, Pilu M and Fisher R B 1999 *IEEE Trans. Pattern Analys. Machi. Intellig.* **21** 476